Scripta Materialia 183 (2020) 144–148

Contents lists available at ScienceDirect

Scripta Materialia

journal homepage: www.elsevier.com/locate/scriptamat

Effect of aging treatment on apparent hydrogen solubility and trapping in a new generation maraging steel

Camille Rousseau[a,b,c,*], Abdelali Oudriss[a,*], Remy Milet[a], Xavier Feaugas[a], Mohamed El May[b], Nicolas Saintier[b], Quentin Tonizzo[c], Mariem Msakni-Malouche[c]

[a] LaSIE, La Rochelle Université, UMR CNRS 7356, Avenue Michel Crépeau, 17042 La Rochelle, France
[b] I2M, Arts et Métiers Campus de Bordeaux-Talence, UMR CNRS 5295, Esplanade des Arts et Métiers, 33400 Talence, France
[c] Safran Aircraft Engines, Site d'Evry-Corbeil, Rue Henri Auguste Desbruères, 91003 Evry Cedex, France

ARTICLE INFO

Article history:
Received 19 December 2019
Revised 18 February 2020
Accepted 10 March 2020

Keywords:
Maraging steel
Intermetallic precipitate
Carbide
Hydrogen

ABSTRACT

New generation maraging steel developed by the aeronautical industry meet the highest mechanical standards thanks to the controlled growth of M_2C carbides and B2-NiAl precipitates during aging treatment at around 500 °C. However, the literature has reported a low resistance of precipitation-hardened steel to hydrogen embrittlement that is associated with aging treatment and trapping at precipitates or reverted austenite. Thus, in relation to the complex microstructure of X23NiCoCr 13-6-3 maraging steel, hydrogen solubility and trapping was investigated using Thermodesorption Spectroscopy. A high apparent solubility of hydrogen was observed after aging that was attributed to reversible trapping at coherent B2-NiAl precipitates.

© 2020 Acta Materialia Inc. Published by Elsevier Ltd. All rights reserved.

Due to its high strength-to-weight ratio, precipitation-hardened martensitic steel is an ideal material for building the structural parts of airplanes. However, these structures must withstand harsh conditions throughout the life of the aircraft, which can include exposure to a corrosive environment if there are defects in protection. Interactions between deformation, microstructure and corrosion reactions may lead to early failure of a structure induced by complex damage mechanisms [1–3]. Thus, they must be clarified and quantified to guarantee structure reliability over a long service life.

A particular concern for high-strength steel is the production of hydrogen from corrosion reactions [3]; structures containing hydrogen may then suffer hydrogen embrittlement (HE). In that case, brittle intergranular failure is generally observed, and is attributed to hydrogen trapping at prior austenite grain and lath interfaces [4–6]. However, for precipitation-hardened martensitic steels, a significant effect of aging on HE resistance has been noticed. Hydrogen can be trapped at semi-coherent or incoherent precipitates and reverted austenite in the case of over-aging, decreasing interface trapping [6–9]. A homogeneous distribution of strong traps such as precipitates within the microstructure then increase the apparent resistance to HE. Recently, Li and coworkers [9] have highlighted the primary role of precipitates on HE resistance for conventional maraging steel. Although they found a fine and homogenous lath structure, PH13-8 was less resistant to hydrogen than 17-4PH. Due to their low misfit with the martensitic matrix, B2-NiAl precipitates in PH13-8 had a lower capacity to trap hydrogen than the incoherent Cu-rich precipitates in 17-4PH. In the same way, aging treatment is a key parameter in the resistance to HE of secondary-hardening steels, which is linked with hydrogen reversible trapping around M_2C carbides [10].

In recent decades, new generation of maraging steel with a low carbon content have been developed by the aeronautical industry. Very high mechanical resistance (UTS = 2200 MPa at 293 K) can be reached thanks to a combination of the typical B2-NiAl fine precipitation of conventional maraging steel with the growth of M_2C carbides, as is the case with secondary-hardening steels [11]. Considering the above, aging treatment would be expected to have a significant influence in their resistance to HE. However, the role of each type of precipitate on apparent hydrogen solubility and trapping must be investigated, as mentioned recently in a review published by Martin et al. [12].

In this paper, the material under study was the new generation X23NiCoCrMoAl 13-6-3 maraging steel. It was elaborated under a vacuum and remelted using a consumable electrode. After a solution treatment at 1173 K, the steel was quenched, and a subzero

* Corresponding authors at: LaSIE, La Rochelle Université, UMR CNRS 7356, Avenue Michel Crépeau, 17042 La Rochelle, France
E-mail addresses: camille.rousseau@ensam.eu (C. Rousseau), abdelali.oudriss@univ-lr.fr (A. Oudriss).

https://doi.org/10.1016/j.scriptamat.2020.03.013
1359-6462/© 2020 Acta Materialia Inc. Published by Elsevier Ltd. All rights reserved.

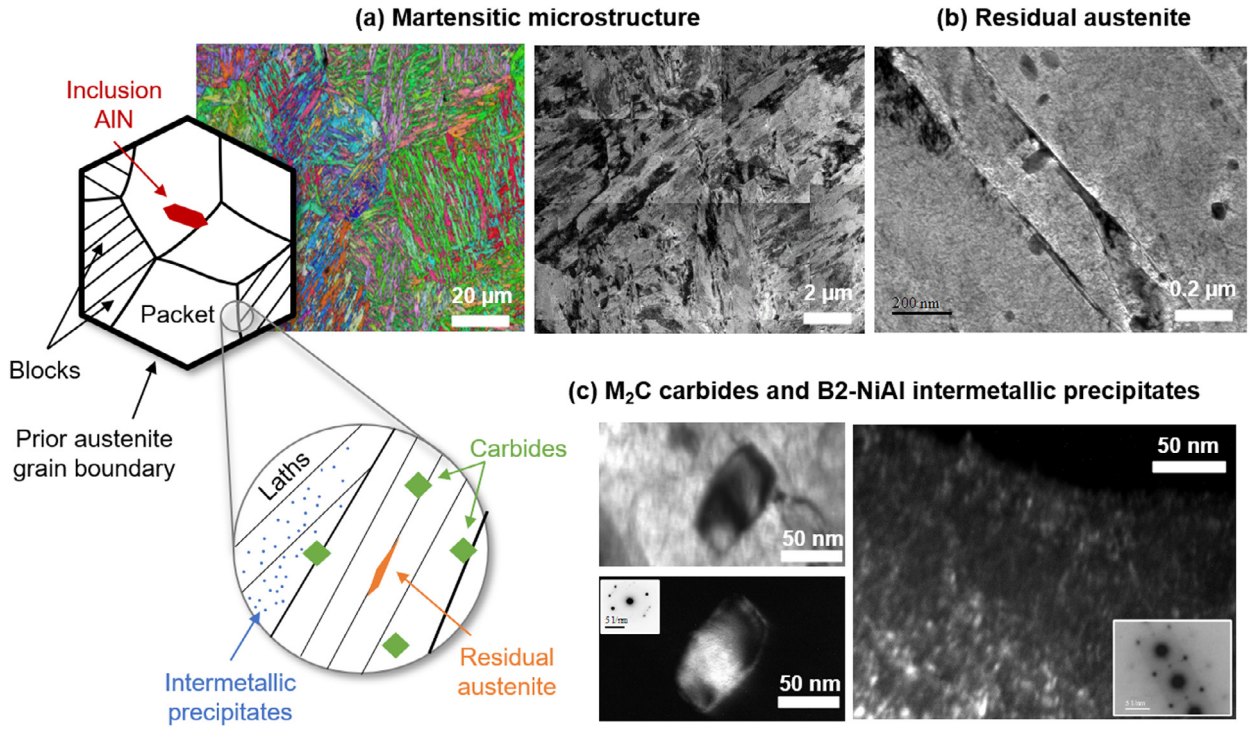


Fig. 1. (a) Schematic view of X23NiCoCrMoAl 13-6-3 maraging steel microstructure. (b) SEM-EBSD (left) and TEM (right) panorama. (b) Residual austenite observed by TEM at lath boundaries. (c) On the left, bright and dark field TEM observations of a M2C carbide. On the right, nanometric B2-NiAl precipitates observed by TEM in dark field.

treatment performed to maximize martensitic transformation. The structure was then relaxed by a short heat treatment at 473 K. Finally, the steel was aged for 10 h at around 773 K.

The microstructure was characterized at different scales, before and after aging, using a Leica DM6000M optical microscope, by scanning electron microscopy (SEM Philips FEI, Quanta 200FEG/ESEM, 20 kV) associated with electron back scattering diffraction (EBSD), and by transmission electron microscopy (TEM JEOL JEM 2011 200 kV). The methodologies have been detailed in previous studies [13].

Fig. 1a shows a schematic view of the martensitic microstructure and heterogeneities of the steel after aging. After quenching and relaxing, a homogeneous martensitic structure was obtained, made of 200 nm-wide laths organized in blocks and packets within equiaxed prior austenite grains of 30 µm (Fig. 1b). No effect of aging treatment on the martensitic structure was noticed. Based on high resolution XRD measurement, both unaged and aged steel contained around 4%–5% of austenite. TEM observations with diffraction pattern analyses showed the existence of fine austenite phases between martensite laths before and after aging (Fig. 1c). Thus, the austenite is only a residual from quenching. The steel also contained around 10 inclusions per mm², which were mainly aluminum nitride (AlN) inclusions of approximately 5 µm in equivalent diameter.

The martensitic steel was hardened by secondary M_2C carbides that grew mainly during the aging treatment. Before aging, M_2C (M=Mo, Fe, Cr), $M_{23}C_6$ and VC carbides were observed by TEM, with an equivalent diameter of 24.5 ± 10.3 nm, and a density of $38 \pm 13\,\mu m^{-3}$ (f_v(carbides) = 0.03%). They were mainly semi-coherent with an average mismatch of around $\delta = 3.7\%$ ($(a_\delta - a_P)/a_\delta$ with a_δ and a_P the phase and precipitate lattice parameter, respectively). In the aged material, the carbides were incoherent or semi-coherent M_2C with an average mismatch of around δ = 2.9%. They were spherical or elongated and had an average equivalent diameter of 35.1 ± 13.1 nm. A total density of $75 \pm 15\,\mu m^{-3}$ was observed (f_v(carbides) = 0.17%) (Fig. 1d). Consequently, aging treatment promoted the nucleation (volume fraction) and growth (diameter) of carbides and then decreased the solutes in solution (substitutional and interstitial states). Aging treatment also allowed the simultaneous growth of spherical intermetallic B2-NiAl precipitates with a diameter of 4.4 ± 0.6 nm, characterized by a high coherency with the martensitic structure and a low mismatch parameter δ = 1.47%. Due to their very small size, the density of NiAl precipitates was difficult to estimate by conventional TEM, but this density should be least a 10-times higher than that of carbides [14]. Other authors found $f_v(B2-NiAl) = 5\%$ and $f_v(B2-NiAl) = 7.2\%$ on similar maraging steel with respectively 0.9 wt% and 1.05 wt% of Al [11,15]. In the present study, high magnification TEM pictures were used to estimate this fraction after aging $f_v(B2-NiAl)$ at around 12% (Fig. 1d).

The high number of interfaces and heterogeneities suggested a high density of dislocations and significant internal stress. From XRD measurements based on a Williamson-Hall analysis [16], the total density of dislocations was estimated at $2 \times 10^{15} m^{-2}$ and the internal stress at 925 MPa. No significant difference was observed before and after aging. TEM measurements and the line-intercept method showed that the intra-granular dislocation density was $14.9 \pm 1.4 \times 10^{14} m^{-2}$ before and $15.3 \pm 2.6 \times 10^{14}\ m^{-2}$ after aging. The geometrically necessary dislocation density was estimated from EBSD measurements [17] to be $4.0 \pm 1.2 \times 10^{14}\ m^{-2}$ before and $1.6 \pm 0.2 \times 10^{14}\ m^{-2}$ after aging. Thus, aging treatment only had a moderate impact on the total dislocation density.

Apparent hydrogen solubility and trapping were then studied on the material before and after aging using Thermodesorption Spectroscopy (TDS). Specimens ($4 \times 4 \times 10\ mm^3$) were mechanically polished with SiC grinding paper down to 5 µm, cleaned with acetone and finally masked with a Mecaprex MA2 resin to proceed to one side polarization. Specimens were subjected to a cathodic polarization at $-100\ mA.cm^{-2}$ (HER: Hydrogen Evolution Reaction) in a deaerated 1 M H_2SO_4 solution at 20 °C. These ex-

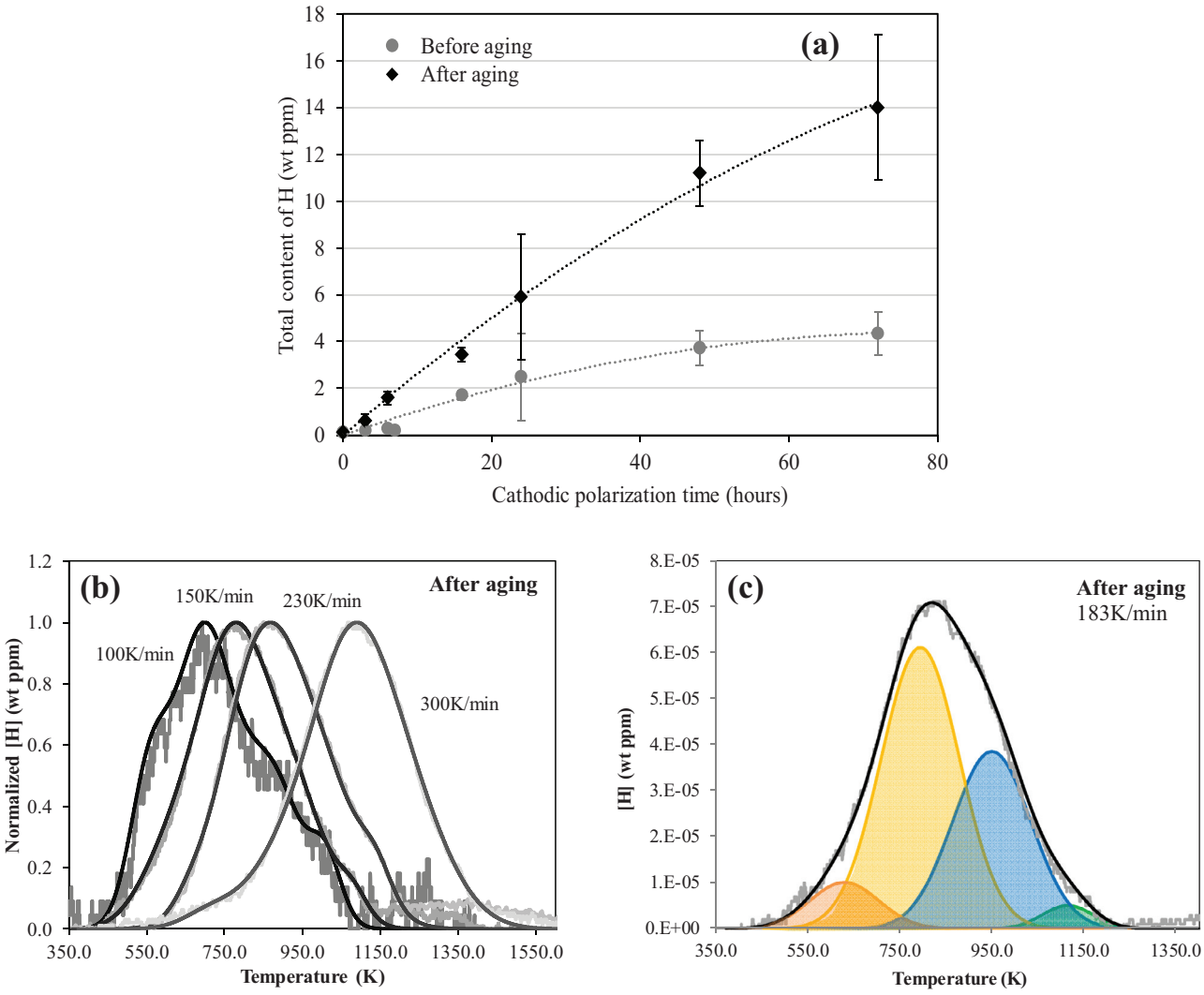


Fig. 2. (a) Apparent hydrogen solubility within the steel before and after aging treatment. (b) Evolution of hydrogen desorption spectra on the aged steel after 24 h of cathodic charging for different heating rate r (c) Deconvolution of a hydrogen desorption spectra performed at 183 K/min on aged steel after 24 h of cathodic charging in four Gaussian peaks. At heating rate r, each peak is associated to the temperature T_p.

perimental conditions were not representative of the actual conditions of the manufacturing and operating environment but allowed to maximize adsorbed hydrogen at the surface. After polarization, the resin was removed, and specimens mechanically polished to remove corrosion products. Finally, a TDS analysis was conducted using gas catharometry with a Jobin Yvon Horiba EMGA-621 W hydrogen analyzer (TCD: Thermal Conductivity Detector).

First, cathodic polarizations were performed for 3–72 h. The total hydrogen content for each charging time was estimated by TDS with direct heating at 2000 °C. As shown in Fig. 2a, the results on the material before aging are consistent with previous studies on martensitic steels [18]. A maximum apparent solubility of around 3 to 4 wppm was obtained after 72 h of cathodic charging. However, hydrogen apparent solubility on the material after aging was higher. After 24 h of cathodic charging, 6 wppm may be introduced into the material without inducing internal damage or blistering. The maximum apparent solubility was obtained after 72 h and was above 10 wppm. Thus, a large quantity of hydrogen may be introduced into the new generation maraging steel X23NiCoCrMoAl 13-6-3 in environments allowing its adsorption onto the surface. This can be explained by the microstructural changes induced by the aging treatment (Fig. 2a).

Following the same methodology, further investigations were performed by polarizing specimens for a fixed time of 24 h and by conducting TDS analysis at specific heating rates (70–300 K min^{-1}) from 80 °C to 2000 °C to obtain desorption profiles. As shown in Fig. 2c, thermal desorption spectra obtained for each heating rate was then deconvoluted using a sum of four Gaussian distributions. Each peak is related to a type of site for hydrogen trapping and a specific temperature for a given heating rate. As has been well established in the literature [19,20], the peaks were moved towards a higher temperature by increasing the heating rate (Fig. 2b). Then, the trapping energy for the hydrogen of the associated type of site is given by Kissinger's equation:

$$\frac{dln\left(\frac{\varphi}{T_{pi}^2}\right)}{d\left(\frac{1}{T_{pi}}\right)} = \frac{-\Delta E_{TL_i}}{R} \quad (1)$$

where φ is the heating rate (K s^{-1}), T_{pi} the i^{th} peak temperature (K), ΔE_{TL_i} the energy of the trap associated with the i^{th} peak and R the gas constant (8.13 J K^{-1} mol^{-1}).

The energy related to the four peaks was 0.12 eV, 0.18 eV, 0.28 eV and 0.50 eV, respectively (Fig. 3b). According to the litera-

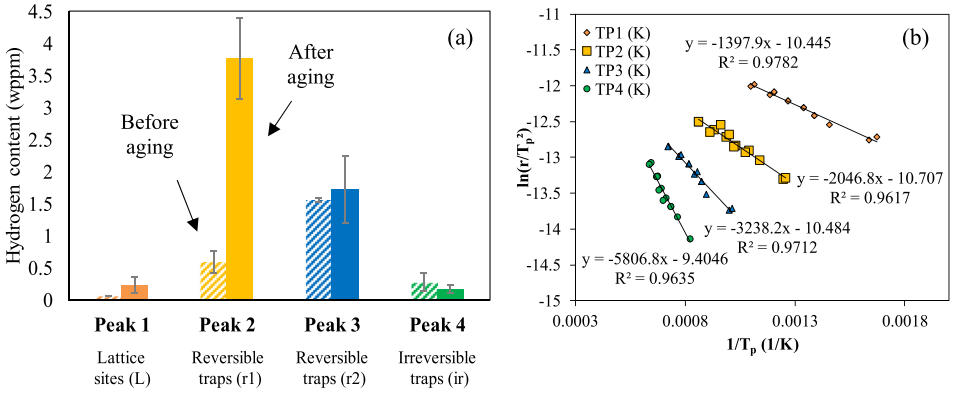


Fig. 3. (a) Hydrogen distribution calculated from deconvolution of desorption spectra for the two states (before and after aging) after 24 h of cathodic charging. (b) Determination of trapping energy associated with each identified peak on the material after aging from Eq (1).

ture [18,21–23], the trapping energy associated with the first peak corresponds to diffusible hydrogen in lattice sites ($\Delta E_{TL} \approx 0.1$ eV). The two intermediate peaks are related to reversible traps ($\Delta E_{TL} \approx$ 0.2–0.4 eV), generally attributed to the elastic field of dislocations and/or coherent and semi-coherent precipitates [24,25]. The last peak can be attributed to irreversible trapping at grain or phase boundaries, dislocation cores and vacancies ($\Delta E_{TL} \geq 0.5$ eV) [22,26].

Regarding the microstructural characterization, both grain boundaries (prior austenite grain, blocks, packets and laths) and phase boundaries (between austenite and martensite) can irreversibly trap hydrogen with an energy $\Delta E_{TL,r}$ of 0.5 eV. Dislocations cores and vacancies within martensite and austenite phases can also act as irreversible traps. Dislocations can contribute to reversibly trap hydrogen in their elastic field, with an energy $\Delta E_{TL,r2}$ of 0.28 eV.

Precipitates can be involved in both reversible and irreversible trapping, and this depends mainly on their coherency [9,10,13,18,24,27]. The exact location of the trapping sites remains unclear (e.g., surrounding strain field, coherent interface, non-coherent interface with misfit dislocations, vacancies in or around the precipitates). However, some results have clearly demonstrated the elastic field contribution to hydrogen trapping at coherent and semi-coherent precipitates [18,28–30]. The local strain field outside the precipitates were caused by the δ mismatch of lattice parameters which exists between coherent or semi-coherent precipitates and the matrix [28,31]. The high coherency of nanometric B2-NiAl precipitates with a martensitic microstructure only generates a low local strain field (δ =1.47%). The first type of reversible traps ($\Delta E_{TL,r1} = 0.18$ eV) could thus be associated with fine intermetallic precipitation. On the other hand, M_2C precipitates are semi-coherent and/or incoherent and could trap hydrogen at local strain fields and at non-coherent interfaces with misfit dislocations or at vacancies in or around the precipitates. They can contribute to both types of reversible traps ($\Delta E_{TL,r1} = 0.18$ eV, $\Delta E_{TL,r2} = 0.28$ eV depending on their coherency, at a surrounded elastic field, and to irreversible traps at dislocation cores and vacancies ($\Delta E_{TL,ir} =$ 0.50 eV).

To evaluate hydrogen distribution within the different sites, the ratio between the peak area obtained from the thermal desorption spectra at medium heating rates (183 K min^{-1} and 230 K min^{-1}) may be considered [32]. The evaluation of hydrogen distribution before and after aging (Fig. 3a) showed that aging is promoting the first type of reversible traps ($\Delta E_{TL,r1} = 0.18$ eV). Indeed, the ratio between the first type of reversible trapped hydrogen C_{Tr1} and diffusible hydrogen C_L is around 9 before aging and around 25 after aging. No modification was observed with aging for the second type of reversible trapped hydrogen C_{Tr2}/C_L and the irreversible trapped hydrogen C_{Tir}/C_L. They were around 10 and 1.5, respectively.

The ratio between reversible trapped hydrogen C_{Tr} associated with local strain, outside coherent and semi-coherent precipitates or induced by edge dislocations, and diffusible hydrogen C_L, can be deduced by analytical calculations Eqs. (2) and (3). For coherent and semi-coherent precipitates, the δ mismatch was used to formalize the reversible trapped hydrogen in their $C_{Tr,prec}$ elastic field as in the following expressions [13,28,31,33]:

$$\frac{C_{Tr,prec}}{C_L} = f_p \frac{\Delta V}{V_p} \frac{1}{\Delta r} \int_{r_p}^{r_p+\Delta r} \frac{s(r)}{s_0} dr$$
$$\text{with } \frac{s(r)}{s_0} = \exp\left(\frac{\sigma_m \overline{V}_H}{k_B T}\right), \ \sigma_m = \left(\frac{E}{1-2\nu}\right)\varepsilon_m$$
$$\text{and } \varepsilon_m = \frac{2}{3}\delta\left(\frac{r_p}{r}\right)^3 \quad (2)$$

Where σ_m and ε_m are the hydrostatic stress and strain, respectively. E is the Young modulus, ν the Poisson coefficient. r_p is the precipitate radius. $\Delta r = r - r_p$ is the radius of the elastic distortion. $\overline{V}_H$ is the partial molar volume, V_p the precipitate volume and ΔV the volume fraction of elastic distortion.

The lattice distortion generated by an edge dislocation induces the creation of an elastic field characterized by a hydrostatic stress. The macroscopic excess of hydrogen resulting from the distortion of crystallographic features can be expressed by the following equation [34–37]:

$$\frac{C_{Tr,dislo}}{C_L} = \frac{\pi \beta^2}{2k_B^2 T^2} \rho \ln\left(\frac{1}{b\sqrt{\rho}}\right)$$
$$\text{with } \beta = \left(\frac{\mu b}{3\pi}\right)\left(\frac{1+\nu}{1-\nu}\right)\overline{V}_H \quad (3)$$

ρ is the dislocation density, b the burgers vector and μ the shear modulus.

As shown in Fig. 4, considering trapping at a local strain around the B2-NiAl precipitates, Eq. (2) gives a $C_{Tr,B2\text{-}NiAl}/C_L$ ratio of around 17, which is in quite good agreement with the experimental value (C_{Tr1}/C_L=25). This result supports the hypothesis that B2-NiAl precipitates constitute the preferential site of reversible trapped hydrogen with a $\Delta E_{TL,r1}$ energy of 0.18 eV and therefore the main source of the difference in apparent solubility between the two states (before and after aging). Applied to the elastic field of carbides, Eq. (2) predicts a $C_{Tr,carb}/C_L$ ratio of around 6 before and after aging. Considering Eq. (3), a lower value was given for trapping at the elastic field of edge dislocations. Indeed, the model predicts a $C_{Tr,dislo}/C_L$ ratio of around 0.1 before and after aging. As shown in Fig. 4, the value associated with carbide was quite sim-

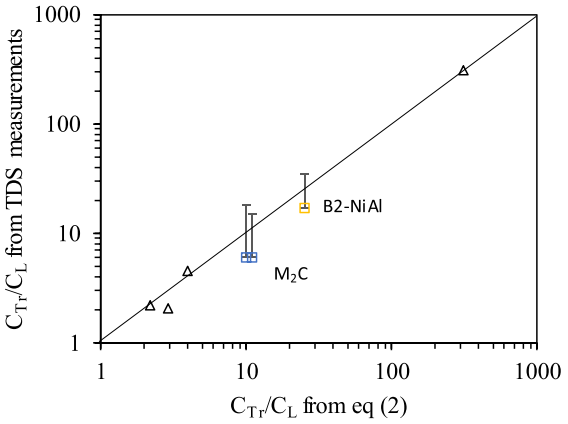


Fig. 4. Comparison between the TDS experimental results and an analytical calculation of CTr,prec/CL from Eq. (2) for the material under study and other results from literature (see *[33] and **[13]).

ilar to the experimental value (C_{Tr2}/C_L=10). Thus, the main factor for the second type of reversible traps ($\Delta E_{TL,r2} = 0.28$ eV) seems to be a consequence of the interaction between hydrogen and carbide precipitation. However, dislocations are expected to have a major contribution on irreversible hydrogen trapping. Indeed, as shown by several authors [37–39], the density of deep traps N_T can be estimated by analytical expressions as a function of dislocation. For the material under study, both dislocations density and irreversible trapped hydrogen C_{Tir}/C_L were found to be constant with aging.

To conclude, a high quantity of hydrogen may be introduced and trapped within the new generation maraging steel. This high apparent solubility can be attributed to the growth of fine precipitates during aging. Our results showed that hydrogen is mainly reversibly trapped at the elastic field induced by coherent fine precipitates with an energy of around 0.18 eV. Semi-coherent carbides also contributed to reversibly trapped hydrogen at their elastic field, with a higher energy (0.28 eV). However, by comparison, the influence of carbides on the apparent hydrogen solubility seems to be more limited. Further investigations are ongoing to study irreversible hydrogen trapping and evaluate the impact of deep trapped hydrogen on the mechanical properties of maraging steel.

The authors would like to acknowledge our colleagues E. Conforto and G. Lotte for their contribution to the TEM and SEM facilities, and R. Millet and C. Berziou for their support with the TDS facilities in the LaSIE Laboratory. We are also grateful to Safran Aircraft Engines for their technical and financial support (Convention CIFRE n° 2017/0988).

Declaration of Competing Interest

The authors declare that they have no known competing financial interests or personal relationships that could have appeared to influence the work reported in this paper.

Acknowledgements

our colleagues E. Conforto and G. Lotte for their contribution to the TEM and SEM facilities, and C. Berziou for his support with the TDS facilities in the LaSIE laborarory.

References

[1] B.F. Brown, in: Stress Corrision Cracking of High Strength Steels Titanium and Aluminum Alloys, Naval Research Laboratory, Washington, D.C., 1972, pp. 1–16.
[2] R.P. Gangloff, in: Corrosion Tests and Standards Manual: Application and Interpretation, ASTM, 1995, pp. 1–20.
[3] J. Venezuela, Q. Liu, M. Zhang, Q. Zhou, A. Atrens, Corros. Rev. 34 (2016) 153–186.
[4] M. Barsanti, M. Beghini, F. Frasconi, R. Ishak, B.D. Monelli, R. Valentini, in: Procedia Structural Integrity, Elsevier B.V., Pisa, 2018, pp. 501–508.
[5] M.J. Gomes da Silva, J.L. Cardose, D.S. Carvalho, L.P.M. Santos, L.F.G. Herculano, H.F.G. de Abreu, J.M. Pardal, Int. J. Hydrogen Energy 44 (2019) 18606–18615.
[6] S. Shen, X. Li, P. Zhang, Y. Nan, G. Yang, X. Song, Mater. Sci. Eng. A 703 (2017) 413–421.
[7] B.G. Pound, Corros. Sci. 42 (2000) 1941–1956.
[8] L.W. Tsay, M.Y. Chi, Y.F. Wu, J.K. Wu, D.-.Y. Lin, Corros. Sci. 48 (2006) 1926–1938.
[9] X. Li, J. Zhang, Q. Fu, E. Akiyama, X. Song, S. Shen, Q. Li, Mater. Sci. Eng. A 742 (2019) 353–363.
[10] D. Li, R.P. Gangloff, J.R. Scully, Metall. Mater. Trans. A 35A (2004) 849–850.
[11] F. Pettinari-Sturmel, B. Kedjar, J. Douin, C. Gatel, D. Delagnes, A. Coujou, Mater. Sci. Eng. A 576 (2013) 290–297.
[12] F. Martin, X. Feaugas, A. Oudriss, D. Tanguy, L. Briottet, J. Kittel, Mechanics - Microstructure - Corrosion Coupling, 1st edition, ISTE Press - Elsevier, 2019, pp. 171–197.
[13] S. Frappart, X. Feaugas, J. Creus, F. Thebault, L. Delattre, H. Marchebois, J. Phys. Chem. Solids 71 (2010) 1467–1479.
[14] D. Delagnes, F. Pettinari-Sturmel, M.H. Mathon, R. Danoix, F. Danoix, C. Bellot, P. Lamesle, A. Grellier, Acta Mater. 60 (2012) 5877–5888.
[15] F. Danoix, R. Danoix, J. Akre, A. Grellier, D. Delagnes, J. Microsc. 244 (2011) 305–310.
[16] T. Ungár, A. Borbély, Appl. Phys. Lett. 69 (2006) 1–4.
[17] J. Pešička, R. Kužel, A. Dronhofer, G. Eggeler, Acta Mater. 51 (2003) 4847–4862.
[18] S. Frappart, A. Oudriss, X. Feaugas, J. Creus, J. Bouhattate, F. Thébault, L. Delattre, H. Marchebois, Scr. Mater. 65 (2011) 859–862.
[19] W.Y. Choo, J.Y. Lee, Metall. Trans. A 13A (1982) 135–140.
[20] J.Y. Lee, S.M. Lee, Surf. Coat. Technol. 28 (1986) 301–314.
[21] C.A. Wert, Springer, Berlin, Heidelberg, 1978, pp. 305–330.
[22] W.A. Counts, C. Wolverton, R. Gibala, Acta Mater. 58 (2010) 4730–4741.
[23] D.E. Jiang, E.A. Carter, Phys. Rev. B 70 (2004) 1–9.
[24] F. Wei, K. Tsuzaki, Scr. Mater. 52 (2005) 467–472.
[25] S. Taketomi, R. Matsumoto, N. Miyazaki, Acta Mater. 56 (2008) 3761–3769.
[26] R. Matsumoto, M. Riku, S. Taketomi, N. Miyazaki, Prog. Nucl. Sci. Technol. 2 (2011) 9–15.
[27] K. Kawakami, T. Matsumiya, ISIJ Int. 52 (2012) 1693–1697.
[28] A. Oudriss, S. Frappart, E. Legrand, J. Bouhattate, J. Creus, C. Savall, X. Feaugas, in: Proceedings of the Steely Hydrogen Conference, Ghent, 2011, pp. 261–272.
[29] M. Shmulevitsh, J. Mater. Sci. 50 (2015) 4970–4979.
[30] M. Shmulevitsh, S. Ifergane, N. Eliaz, R.Z. Shneck, Int. J. Hydrogen Energy 44 (2019) 31610–31620.
[31] B.D. Craig, Acta Metall. 25 (1977) 1027–1030.
[32] A. Oudriss, A. Fleurentin, G. Courlit, E. Conforto, C. Berziou, C. Rébéré, S. Cohendoz, J.M. Sobrino, J. Creus, X. Feaugas, Mater. Sci. Eng. A 598 (2014) 420–428.
[33] F.G. Wei, K. Tsuzaki, Metall. Mater. 37A (2006) 331–353.
[34] J.P. Hirth, B. Carnahan, Acta Metall. 26 (1978) 1795–1803.
[35] J.P. Hirth, J. Lothe, in: Theory Dislocations, (2nd ed., Krieger Publishing Company, 1982, pp. 506–509.
[36] W.G. Wofler, M.I. Baskes, Acta Metall. 33 (1985) 2005–2011.
[37] T.A.K. Al-Nahlawi, B.J. Heuser, Scr. Metall. Mater. 32 (1995) 1619–1624.
[38] A. Turk, D. San, P.E.J. Rivera-díaz-del-castillo, E.I. Galindo-nava, Scr. Mater. 152 (2018) 112–116.
[39] J. Creus, S. Frappart, G. Courlit, C. Berziou, E. Conforto, X. Feaugas, F. Thebault, L. Delattre, ASME Press, Grand Teton National Park, Wyoming, USA, 2012, pp. 563–573.